International Journal of Material Forming (2022) 15:45
https://doi.org/10.1007/s12289-022-01695-3

ORIGINAL RESEARCH

Robustness of deep-drawing finite-element simulations to process variations

Kelin Chen[1] · Alexander Breunig[2] · Jinjin Ha[3] · Brad L. Kinsey[3] · Peter Groche[2] · Yannis P. Korkolis[1]

Received: 22 September 2021 / Accepted: 20 April 2022

Abstract
Robustness of numerical models paves the way for efficient compensation of perturbations resulting in deviations from the nominal conditions. This is critical if the numerical simulations will be used to determine closed-loop process control adjustments to assure the final part quality. This work details the procedure to establish and validate numerical process models, through an investigation of deep-drawing of AA1100-O blanks using 3D Servo Press. Of particular interest is the robustness of the deep-drawing simulation models to different process variations and off-design conditions. The experiments are performed on a 3D Servo Press, used as a conventional press, and equipped with a spring-loaded blank holder. From the experiments, the punch force–displacement as well as local features, i.e., flange draw-in and wall-thinning, are obtained. Two types of finite element models of the drawing process are created, one using shell and the other using solid elements. Correspondingly, the plastic anisotropy of the blanks is modeled using the Yld2000-2d (2D) and Yld2004-18p (3D) yield functions. The friction coefficient between the blank and tooling is inversely identified by comparing the simulated punch force–displacement response, flange draw-in and thickness variations with the experimental ones. The robustness of the numerical and material models is confirmed by process variations on the geometry of the blanks, i.e., an initial offset of blank center and elliptical blanks. However, the wrinkling of the flange due to variation of the blank holder force is not captured by the model. A modification to the model, i.e., by introducing appropriate geometric imperfections to the blank, enables it to predict the flange wrinkling. This work investigates the robustness of numerical models to different types of process variations, which is vital in model-based control analyses.

Keywords Deep-drawing · Friction · Anisotropy · Robustness · Process variation · Wrinkling · Process control

Introduction

Finite-Element (FE) simulation is an established tool for the efficient design of deep-drawing processes and systems. It can detect process limits like wrinkling, tearing and wear, and guide process and tooling design. Typically, simulations make use of the nominal parameter values of the process and system design. Based on the prediction, the process or system can be modified and rechecked in a new version of the process simulation.

In order to obtain accurate FE simulation results, construction of an appropriate FE model is necessary. It is composed of constitutive models to describe the material response to loads, geometrical description of the process, boundary conditions, contact behavior between tools and workpiece, temperature increase due to energy dissipation, etc. Constitutive models used in FE simulations consist of mathematical relations for the stresses and strains. They contain material parameters that should be calibrated either based on material characterization experiments or on process and system conditions using an inverse identification procedure [1].

Inherent uncertainties in the FE model are present with respect to the model structure, the parameter values and the numerical approach. Uncertainty in the model structure can

✉ Kelin Chen
chen.9903@osu.edu

[1] Department of Integrated Systems Engineering, The Ohio State University, 1971 Neil Avenue, Columbus, OH 43210, USA

[2] Institute for Production Engineering and Forming Machines, Technische Universität Darmstadt, Otto-Berndt-Str. 2, 64287 Darmstadt, Germany

[3] Department of Mechanical Engineering, University of New Hampshire, 33 Academic Way, Durham, NH 03824, USA

Published online: 03 May 2022

be either traced back to a lack of knowledge about the relevant phenomena, if white or grey models are used, or a lack of data in the case of black or grey models [1, 2].

Uncertainty in the parameters of constitutive models and process exists, if the variation of the values is unknown. This influence on the simulation results of deep-drawing process has been investigated widely, such as the coefficient of friction [3–5], material strain-hardening curve [6], punch speed [3, 7], and plastic anisotropy [5, 6, 8–10].

When the model parameters are calibrated using experiments under various conditions, the uncertainty in the inverse identification methods hinders transparency with respect to the influence of varying process or system conditions. For example, since friction coefficients often used in FE simulations are derived from an inverse identification method, the uncertainty arising from this approach is not well defined. Uncertainty regarding the model structure and the parameter values is controlled by validation procedures.

The FE model used in the simulations can also cause uncertainty. This kind of uncertainty can be reduced to an acceptable degree by well-established verification procedures. With respect to deep-drawing simulations, the influences of element type [6, 11], element size/mesh density [12], integration point, and contact properties [11, 13] have been studied extensively.

Since the initial process parameters for the FE simulations are set up with nominal values, the FE predictions can differ from the experimental observation of the real process due to uncertainties mentioned. As a consequence, the process design has to ensure that the process outcome is expedient even under varied process and system conditions. To achieve this goal, two approaches regarding process robustness and model-based process control have gained interest.

Robustness [14] aims at a minimized deviation of the process result, even if the deviations in parameter values are maximized. So far, to the best knowledge of the authors, a validation procedure for systematically establishing the robustness of a FE model of a forming process is not documented in the literature. The paper at hand proposes implementable procedures for process validation and presents results for a deep-drawing problem. A validated model can construct a sound basis for robustness investigations in the FE simulation, using strategies like design of experiments (DOE) or the Monte-Carlo method.

An extended validation of the process model requires a comparison of results from experiments and simulations at different set-points. Deep-drawing experiments with different tool geometries or tool surfaces are expensive. Consequently, the extended validation approach should make use of easy to achieve set-points. This paper describes different set-points efficiently achievable and demonstrates the necessity of the extended validation process for robustness and control investigations in deep-drawing.

The validation procedure itself needs parameters that can be reliably compared between the simulation and experiment results. For deep-drawing processes, the draw-in of the flange [4, 15], the punch force–displacement [4–6, 9, 11, 16], the thickness distribution [3–6], the earing profile [6, 9, 11, 17, 18] and the wrinkling wave number [19] have been used for validation purposes. Selected model features and validation metrics from the literature for deep-drawing simulations are presented in Table 1. Given that the sensitivities of the simulations to these parameters are different, the reliability and robustness of a numerical model rely on what models and validation parameters are selected.

The work described in this paper aims to establish a validated and robust numerical model for the simulation of a deep-drawing process, for future model-based control analyses. The structure of the paper is as follows: Sect. 2 presents an introduction of the 3D Servo Press [20] and tooling used for the drawing experiments. FE models for deep-drawing simulations are developed and verified in Sect. 3, and then they are validated based on several selected parameters in Sect. 4. Robustness of the calibrated FE models to process variations is investigated in Sect. 5.

Table 1 Selected model features and validation metric for deep-drawing simulations

		Model features					
		Friction	Anisotropy	Punch speed	Hardening	Contact property	Element selection
Validation metrics	Punch force-displ	[4–6, 9, 11, 12, 15, 16]	[6, 9, 12, 16]	[7, 40]	[6, 18]	[11, 13]	[6, 11]
	Thickness	[3–6, 15]	[5, 6, 16, 19]	[3, 7, 40]		[13]	[6]
	Draw-in	[4, 15]					
	Earing height		[5, 6, 9, 17]		[18]		[11]
	Wave number		[12, 19]				

Experiments

Material

The material of this study is commercially-pure aluminum in its fully-annealed state, i.e., AA1100-O, received as cold-rolled thin sheets of 0.51 mm thickness, initially in -H24 temper. The specimens used in this study (i.e., circular blanks for deep-drawing) were produced by laser cutting. In order to reduce the influence of material handling, e.g., on strain-hardening, the material was annealed after the cutting process at 343 °C for 90 min and left to cool in the air outside the oven (Nabertherm NA 15/65).

3D Servo Press

The press used in the experiments is a 3D Servo Press, which differs from a conventional one. Besides the conventional vertical motion of the ram, additional tilting motions around two axes can be performed, see Fig. 1. This novel forming machine was developed at the Institute for Production Engineering and Forming Machines at the Technical University of Darmstadt [20]. The machine consists of three independent servomotors and kinematic linkages, spaced every 120°. The linkages are coupled at the vertical axis of the machine, to produce up to 40 mm of vertical (z-axis) and up to 4.0° of tilting (about the x- and y-axes) motions of the ram. The force capacity of the machine is 10 kN. It is controlled by a PLC (Bosch Rexroth L65). This machine has been used in previous works to control the product stiffness during incremental forming [21] and to show the influence of closed loop control on the overall machine-stiffness [22].

Tooling

The tooling uses a ball joint with its pivotal point in the tool center point (TCP) (Fig. 2a), which decouples the tilting motion from the vertical ram motion. The cylindrical pins shown in Fig. 2a translate the tilting motion of the ram into a linear motion, which in turn compresses the springs (of stiffness $k = 8.5$ N/mm each) situated below the cylindrical pins. This converts the vertical motion of the cylindrical pins into a force. As the cylindrical pins can be moved individually, each of the eight springs is capable of producing an individual force, which can be used to apply a local blank holder pressure as demonstrated in previous work [23]. It should be noted that due to the vertical motion of the ram, the springs are compressed throughout the whole forming process and not only when the ram is tilted. This results in a linearly increasing blank holder force (BHF) as the punch displacement increases during the process. During forming, the punch and BH forces are measured with piezoelectric force transducers, located as in Fig. 2b.

A schematic of the tooling geometry used in these tests is given in Fig. 2c. The punch nose and die fillet radii are both $R = 2$ mm, while the clearance between the punch and die is $c = 0.65$ mm or 1.3 times the undeformed blank thickness (Fig. 2c). The tool is made from 1.2379 high-alloy steel, surface hardened to a hardness of 62 HRC and ground-finished to a surface roughness of $R_z = 2$.

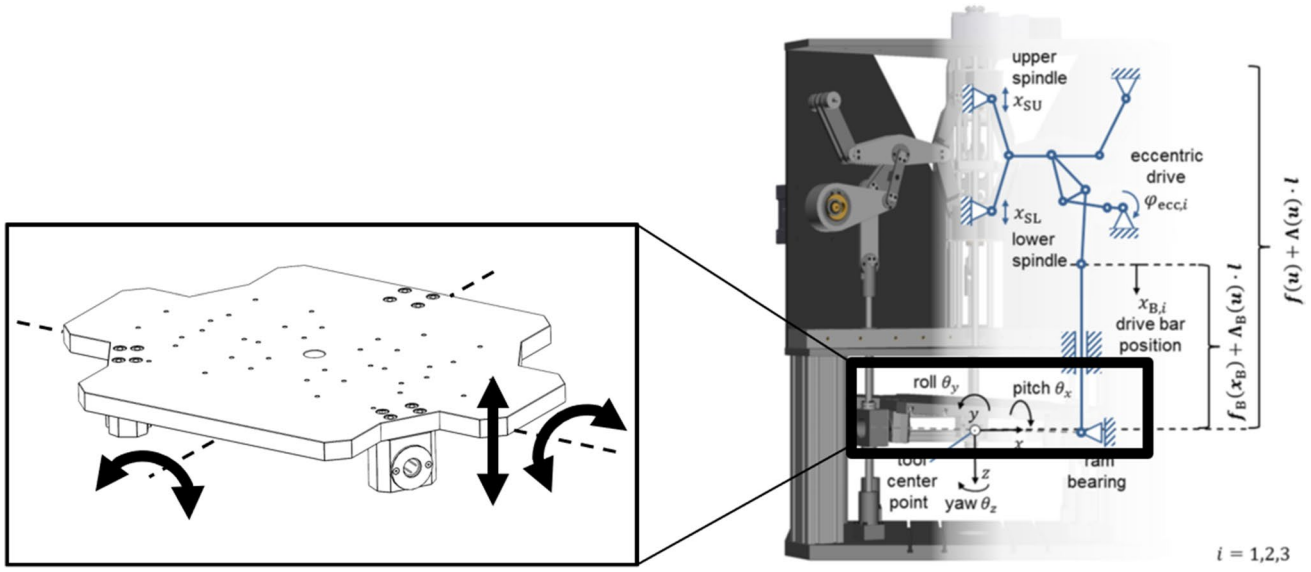

Fig. 1 Schematic of the 3D Servo Press [42], also showing the three degrees of freedom of the press ram

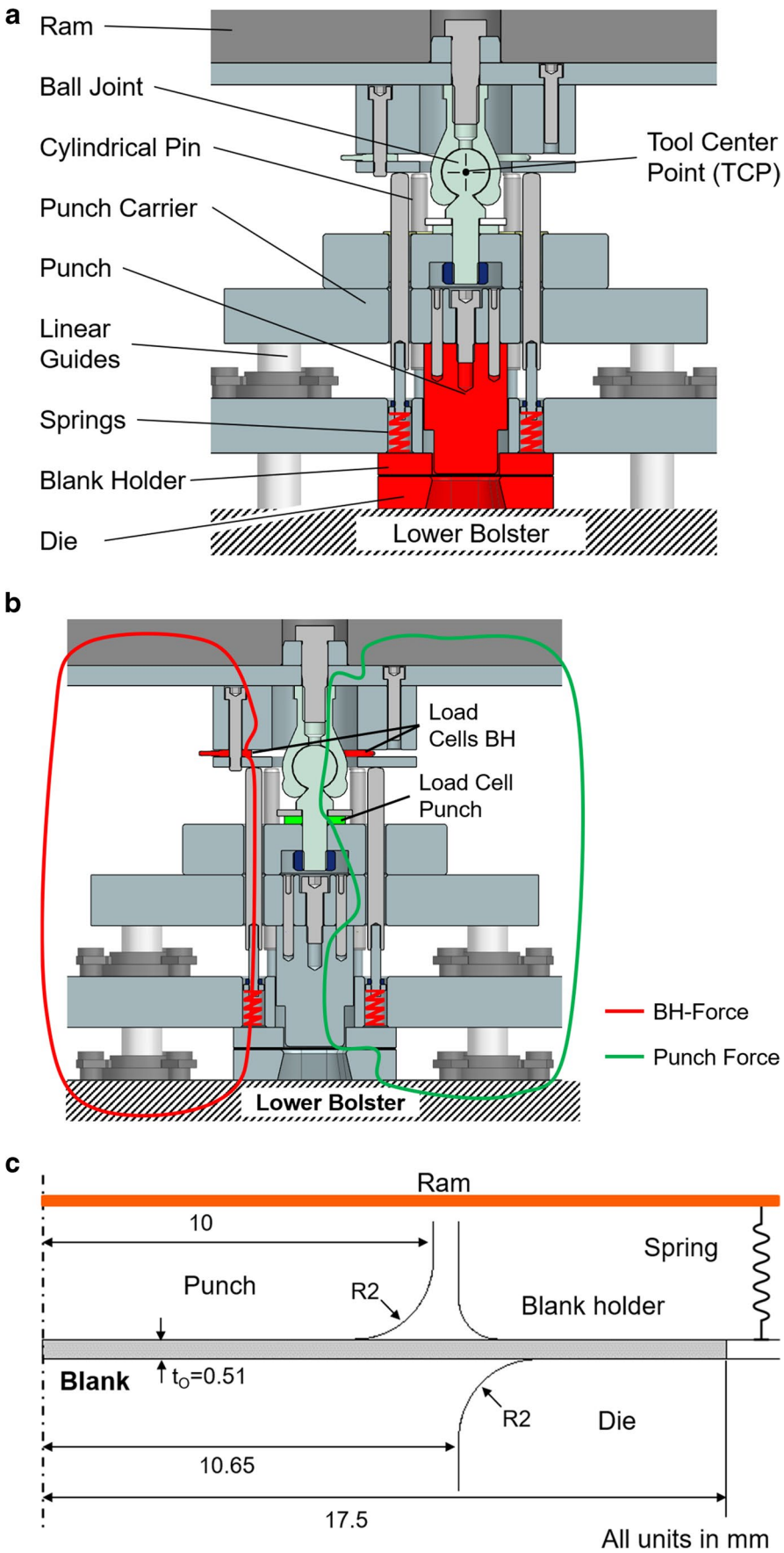

Fig. 2 (a) Schematic of the tooling; (b) flow of forces in the tooling; the load cells are identified; (c) geometry of the tooling (using symmetry)

Drawing experiments

The cups are drawn from a blank of an initial diameter D= 35 mm using a punch with diameter d_0= 20 mm, resulting in a draw-ratio of $\beta = \frac{D}{d_0} = 1.75$. Because of the draw-ratio, it is possible to fully-draw these cups using the spring-loaded BH. The drawing of the experiments is performed with punch speeds between 0.5 – 4 $\frac{\text{mm}}{\text{s}}$. During the experiments, all blanks are lubricated with a commercially available prelube (Multidraw PL 61 SE by Zeller + Gmelin). The lubricant is manually applied to the blanks using a cloth. In order to achieve repeatable lubrication states, an abundance of lubrication is applied to each of the blanks.

Three families of experiments are performed, as shown in Fig. 3. In the first two photos, cups drawn without a BH, or with only the self-weight of the BH are shown, respectively. Excessive wrinkling of the cup flange is observed in both cases, as expected. These experiments are terminated early, to avoid damage to the tooling from ironing the wrinkles. In the last photo, a cup drawn using the spring-loaded BH is shown. In every case, 5 tests were performed and good repeatability is observed, both for the shapes, and the punch force–displacement curves. The error of the maximum force is about 3%. The punch force–displacement responses of all repeated tests can be found in the Supplementary Information.

Measurements

Sensors and data acquisition

In order to precisely quantify the experimental results, the tool is equipped with sensor systems in order to measure the punch displacement and force, as well as the BHF. In particular, the following sensors are used:

- Punch displacement1x Linear Resistive Transducer (Burster 8713–50)
- Punch force1x Piezoelectric force transducer (HBM CLP 62 kN)
- BH force3x Piezoelectric force transducer (Kistler 9012-A)

A charge amplifier (Kistler 5073–4) is used to convert the charge by the piezoelectric sensors to a voltage signal. All process data is fed into an analog-to-digital converter of the 3D Servo Press, where the voltage signals are translated into force/displacement data and finally transferred to a PC to be recorded with custom software created using National Instruments LabVIEW.

As piezoelectric force transducers need to be preloaded with a screw (see Fig. 2b), when applying a compressive force to the structure surrounding the sensor, part of that force is not transferred through the load cell, but the screw instead. To compensate for this, the screws are first tightened to a predefined level of 7 kN for each of the BH sensors and the punch-sensor. Then, the sensor assembly is placed in a compression testing machine (Zwick Roell Allround-Line 100 kN) and loaded with known forces. As expected, the force observed by the piezoelectric sensors is lower than the known force applied by the compression testing machine. With this information the correction factors, i.e., $\alpha = \frac{F_{\text{Compression}}}{F_{\text{Piezo}}}$, are determined to be α_{Punch}= 1.33 and α_{BH}= 1.10.

Thickness and draw-in measurements

In order to obtain the thickness of the drawn cup, the specimens are individually embedded in an epoxy resin, see Fig. 4a. After hardening, the epoxy cups are first turned to remove any excess resin around the specimen. After this, the resulting "pucks" are aligned on a milling machine, in such a way that the rolling direction (RD) is oriented horizontally. Subsequently, the embedding material is shaved off with a milling tool, until the tool slightly grazes the outer edge of the vertical part of the cup (Fig. 4b). This procedure is repeated on the opposite side (Fig. 4c), so that the overall distance from the parallel surfaces can be measured on the milling machine and precisely half of the sample can be milled away (Fig. 4d). The cut is then polished, and black and white photos are taken with a Zeiss Smartzoom 5 digital microscope. These images are then processed with a medial axis algorithm in Python, and the thickness and draw-in length are obtained, to be compared with the numerical

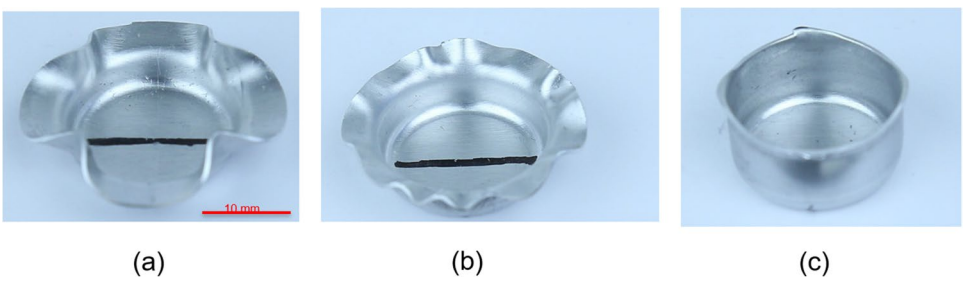

Fig. 3 Photos of drawn cups with three different blank holder force (BHF) settings: (a) zero BHF; (b) 55 N BHF; (c) spring-loaded BH

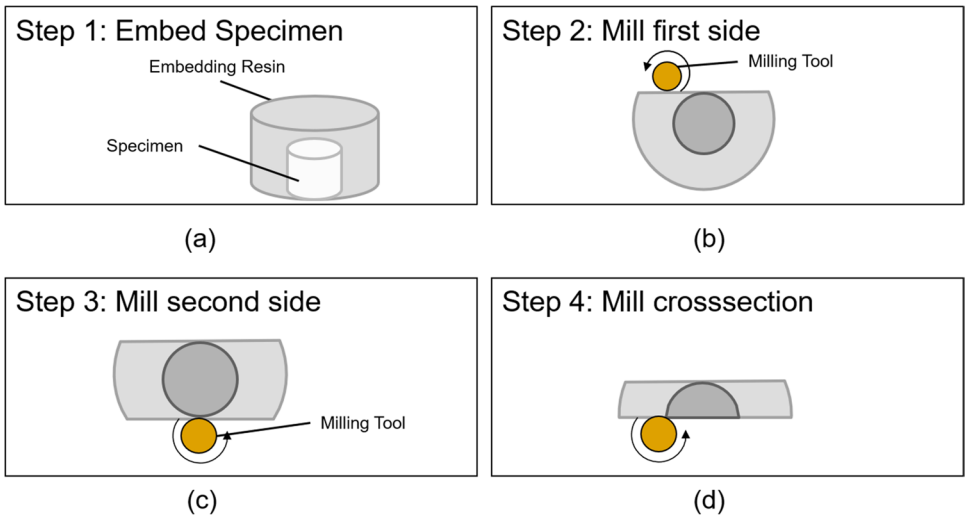

Fig. 4 Schematics of the embedding and cutting procedure to measure the thickness of the drawn cups

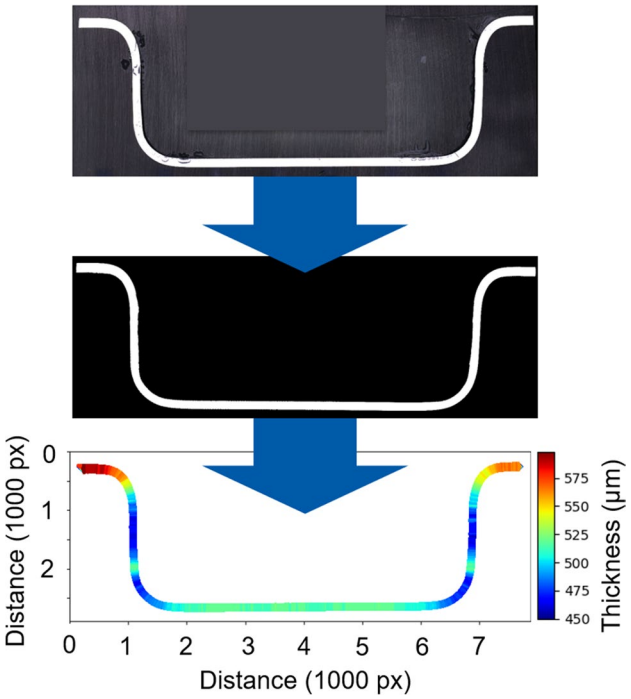

Fig. 5 Thickness distribution of a drawn cup cut along the rolling direction, at the punch displacement of 8 mm

results. As most of the specimen is destroyed during this procedure, each cup can only be used for one dataset.

Figure 5 shows typical results from this procedure, including the wall thickness profile measured. As expected, the bottom of the cup shows minimal thinning, while the partially-drawn flange shows significant thickening (over 12%). The maximum thinning occurs around the punch corner radius, as expected [5, 24]. At this intermediate stage of drawing, similar levels of thinning are observed in the vertical cup walls on both sides of the cup. Recall that these cups were successfully drawn, so no excessive thinning is observed.

Numerical simulations

Material model

Strain-hardening

The plasticity and formability of the material of this study has been reported in detail in [25]. Here, for completeness, only a summary is provided. Uniaxial tension tests were conducted to characterize the strain-hardening response of the AA1100-O sheets. ASTM E8 uniaxial tension specimens [26] were cut along the RD of the sheet and tested using a MTS universal testing machine. Details about the dimensions of the specimen and the test setup can be found in [25]. The material exhibits an initial yield stress of about 40 MPa and the uniform strain in the test section reaches about 23% before the specimen develops necking. Textbook values for the elastic properties, i.e., 70 GPa for the Young's Modulus and 0.3 for Poisson's ratio, are adopted in the simulations. Due to the infinitesimal nature of elastic strains in comparison with the total strains, the material is assumed elastically isotropic in the simulations. To facilitate the numerical simulations in the large strain regime, the hardening response is extrapolated using the Voce isotropic hardening law (see Fig. 6).

Yield function

The AA1100-O sheet exhibits plastic anisotropy, which is demonstrated by the different uniaxial tension responses of specimens cut along difference orientations. To capture the anisotropic behavior of the sheets, the plane stress

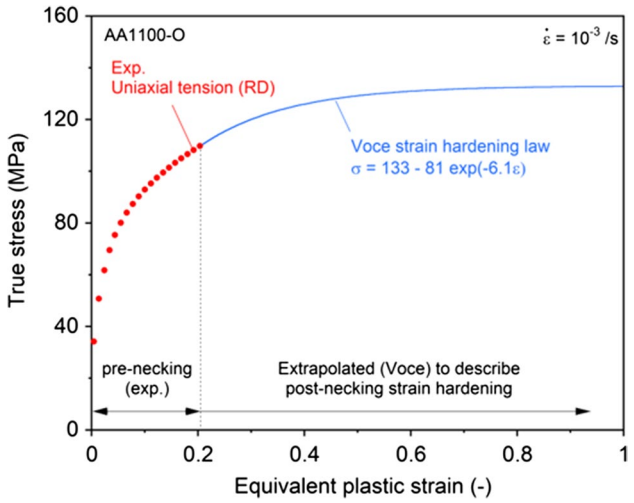

Fig. 6 Uniaxial true stress–strain response of a coupon specimen cut along the rolling direction of the material. Included is the extrapolation using Voce hardening model [25]

Yld2000-2d [27] and fully-3D Yld2004-18p [28] anisotropic yielding functions are adopted for this study. The Yld2000-2d model has 8 parameters, and Yld2004-18p model has 18 parameters to be identified. Seven uniaxial tension, a disc compression, and three plane strain tension experiments were conducted to characterize the plastic anisotropy and calibrate the material parameters [25]. These 11 experiments provide a total of 21 data points, see Table 1 of [25], to calibrate the two yield functions. The stress states and the plastic strain ratios (r-values) for the specimens were evaluated at the plastic work density of 10 MJ/m^3, and an error function for the difference between the experimental and predicted values was generated. The anisotropic parameters in each model were determined by minimizing the error function. The resulting anisotropy parameters are given in Tables 2 and 3.

Figure 7 shows the yield locus of Yld2000-2d (solid lines) and Yld20004-18p (dashed lines) projected onto the rolling and transverse stresses plane at different shear stress levels. It can be seen that both anisotropic yield contours capture the experimental data quite well compared to the von Mises one. It should be noted that since the same set of data were used to calibrate both Yld2000-2d and Yld2004-18p and due to the mathematical nature of both yield functions, the contours of the two functions are almost identical.

Finite element model

Model description

A FE model is developed in the commercial software Abaqus/Standard 2019 (implicit) to simulate the deep-drawing process. The material models of the previous section are implemented into User Material Subroutines (UMATs). The Yld2000-2D and Yld2004-18p yield functions are used in the shell and solid models, respectively, because the former requires a yield function for plane stress (2D) and the latter for full stress (3D). The FE model replicates the 3D Servo Press and forming tooling (see Sects. 2.2 and 2.3), which consists of the ram, connected to the BH with 8 springs (stiffness of 8.5 N/mm for each), the punch, the die and the circular blank (see Fig. 8). The ram, BH, punch, and die are modeled as rigid surfaces in the FE model. Taking advantage of the orthotropic symmetry of the material, only one quarter of the blank is used in the FE model, with appropriate boundary conditions. The quarter model will be later extended to the full model, when symmetry boundary conditions are no longer valid, e.g. when non-periodic wrinkling occurs. Contact between the blank and the tooling (i.e., BH, punch, and die) is assumed to be "hard contact" with a constant friction coefficient. In the "hard contact" formulation, the contact pressure remains zero when the clearance between the two contact surfaces is larger than zero, and it increases drastically when that clearance becomes zero, allowing no penetration. In contrast, in the "soft contact" formulation, the contact pressure starts to increase even when the clearance is positive. Despite the exponential increase, this is less drastic than the hard contact case. A certain amount of penetration is also allowed.

The in-plane mesh of the quarter blank is shown in Fig. 9a. A coarse mesh (600 elements) is generated in the central part of the blank since the deformation is small and

Table 2 Yld2000-2d anisotropy parameters for AA1100-O

α_1	α_2	α_3	α_4	α_5	α_6	α_7	α_8
0.969	1.041	1.025	0.995	1.006	1.003	0.891	0.943

Table 3 Yld2004-18p (3D) anisotropy parameters for AA1100-O

c'_{12}	c'_{13}	c'_{21}	c'_{23}	c'_{31}	c'_{32}	c'_{44}	c'_{55}	c'_{66}
0.982	0.916	0.887	0.801	1.214	1.100	0.986	1.027	0.730
c''_{12}	c''_{13}	c''_{21}	c''_{23}	c''_{31}	c''_{32}	c''_{44}	c''_{55}	c''_{66}
0.978	0.962	1.087	1.034	0.518	0.736	1.007	0.979	1.029

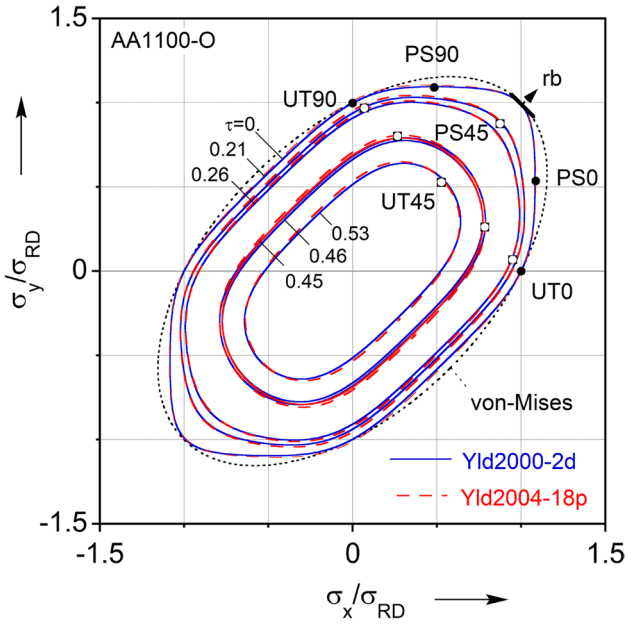

Fig. 7 Yield loci at different shear stress levels, predicted by Yld2000-2d (solid lines) and Yld2004-18p (dashed lines), with experimental data (symbols) used for the parameter calibration. The von Mises locus is also included for comparison

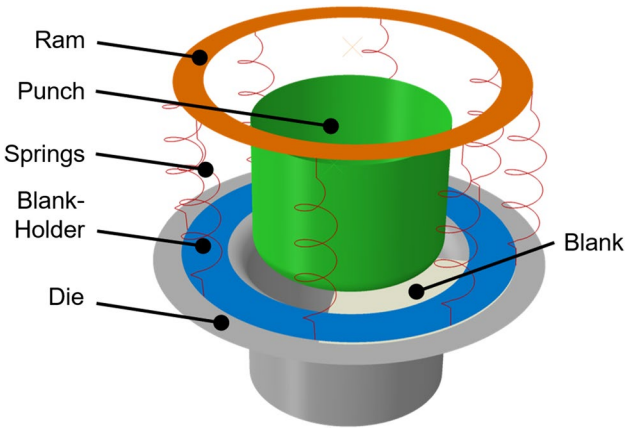

Fig. 8 Finite element model of the tooling, with the major components identified

relatively uniform [29]. A refined mesh of 70 (radial) × 120 (circumferential) elements is used in the annular region of interest, which includes the wall and flange of the drawn cup. (For clarity, the initial positions of the punch and die are identified by the red and blue lines, respectively, in Fig. 9a. Dashed lines are the locations of flat regions on the tooling and solid lines are the projected radius endpoints.) Shell elements are commonly adopted in sheet metal forming process simulations due to their low computational cost compared to solid elements. However, in some cases, e.g., the prediction

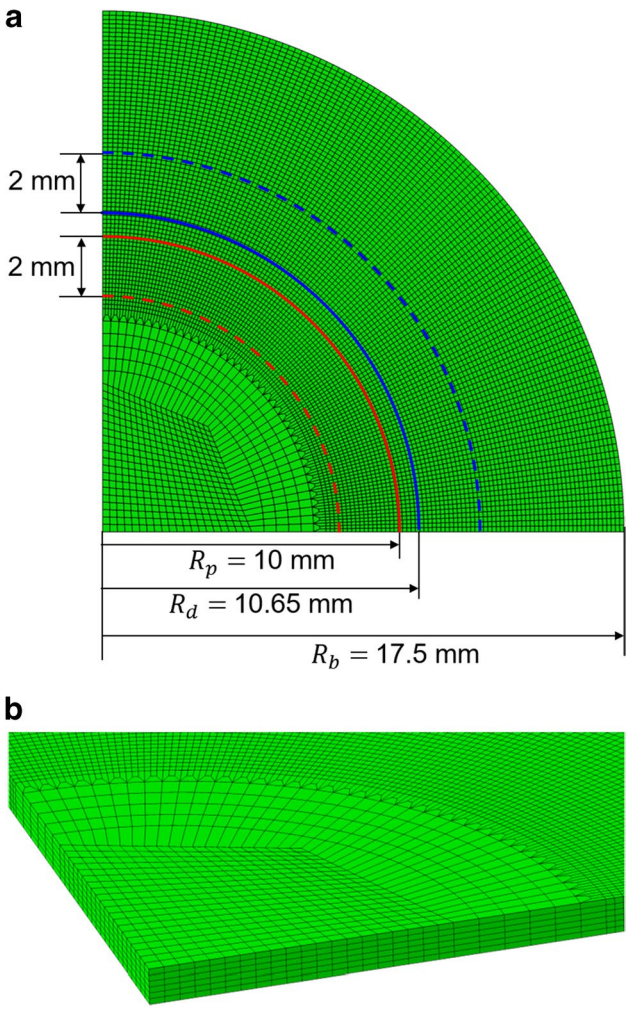

Fig. 9 Finite element mesh of the blank: (a) in-plane mesh of the shell and solid element models; Dashed lines are the locations of flat regions on the tooling and solid lines are the projected radius endpoints. (b) Closer view of the mesh for solid element model

of localized deformation or localized wall thinning in deep-drawing, shell elements do not perform as well as the solid elements. To have a better understanding of the computational efficiency and accuracy for each element option, we have adopted both the solid and shell elements in our simulations. The same in-plane mesh is used for both models. Reduced integration linear shell elements (S4R) and linear solid elements (C3D8R) are adopted in the shell and solid models, respectively. For the solid model, 6 elements are assigned through the thickness of the blank (see magnified view in Fig. 9b). The use of linear elements is dictated by the presence of contact.

The drawing process includes two steps, as in the experiments. First, a BHF 123 N preload, including the self-weight (55 N) of the BH, is applied to the flange of the blank by prescribing a 1.8 mm compressive displacement to the ram before the drawing starts. Second, the same compressive

displacements for the punch and the ram are prescribed, drawing the blank while at the same time linearly increasing the BHF.

Model verification

There is a variety of factors that may affect the simulation results, e.g., mesh density, element order and integration, and choice of hard or soft contact. For both the shell and solid models, these factors are checked and found that they do not affect the results significantly for the base models being used in this work. A mesh convergence study is performed, to assure that a sufficiently high mesh density is present in the models. Quadratic elements cannot be used here, due to the contact. Full or reduced integration elements yield identical results. Finally, no difference in the results is observed when the contact formulation is changed from soft to hard.

Identification of the friction coefficient

A factor that plays a pivotal role in our deep-drawing simulations is found to be the Coulomb friction coefficient between the blank and the tooling. This can be demonstrated by the predicted punch force–displacement responses in the deep-drawing simulations using the solid model, as shown in Fig. 10a, where four friction coefficients that vary from zero to 0.3 are shown as examples. As the friction coefficient increases, the slope of the punch force–displacement response beyond the displacement of 1 mm becomes increasingly larger, which leads to significantly larger maximum punch force. Note that the maximum force for $\mu = 0.3$ is almost twice that for $\mu = 0$. The effect of friction can be further demonstrated by the simulated thickness variation of the partially drawn cup at a punch displacement of 8 mm, as shown in Fig. 10b. The predicted thickness of the blank is plotted against the position along the meridian of the central plane for the same set of friction coefficients used in Fig. 10a. It can be seen that while the thickness at the bottom of the cup is not significantly affected by the friction coefficient, the thickness distribution near the punch corner radius, along the wall and in the flange, does markedly depend on the friction coefficient. On the other hand, the flange draw-in is found to have limited sensitivity to the friction coefficient.

In view of the significant effects of the friction coefficient on the simulation results (Fig. 10), it is crucial to identify the appropriate friction coefficient to be used in the deep-drawing simulations. Since a direct measurement of the friction coefficient in our deep-drawing process is not possible, we chose to identify the friction coefficient using an inverse method, i.e., by comparing the structural response (punch force–displacement) of the simulation with the experiments.

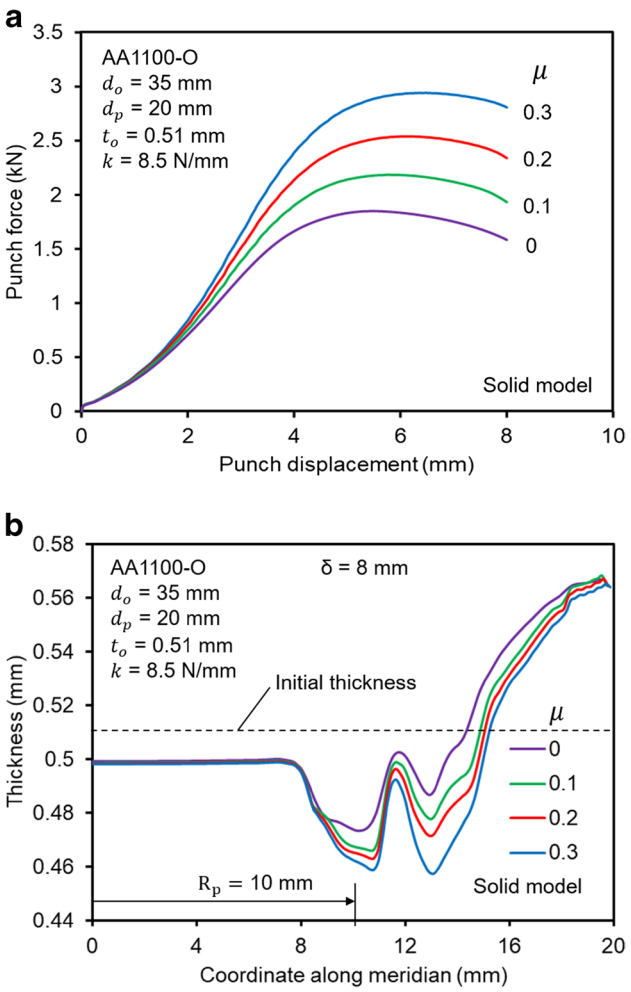

Fig. 10 (a) Predicted punch force–displacement responses with a set of friction coefficients; (b) Predicted thickness distribution of the blank along the meridian of the rolling direction (using symmetry) at the draw depth of 8 mm, with a set of friction coefficients

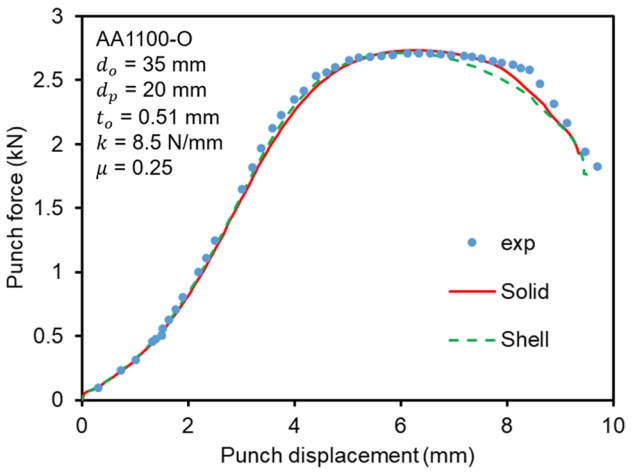

Fig. 11 Punch force–displacement responses from the measurements, and predictions from solid and shell models with a friction coefficient of 0.25

A blank with a diameter of 35 mm is adopted in the identification process.

Figure 11 shows the response from the experiment (blue circles) up to a drawing depth of 10 mm. The punch force increases drastically and reaches the maximum of 2700 N at the punch displacement of about 6 mm. It then drops as the drawing depth continues to increase. A lucid explanation of this effect is provided by [29]. Included are the responses from the solid (solid red line) and shell models (dashed green line), both using the friction coefficient of $\mu = 0.25$. It can be seen that the solid model response matches the stiffness of the early-stage response, the maximum force and the post-max. load response, all quite well. The prediction of the shell model also shows good agreement with the experiment, except that the post-limit load response is slightly lower. The comparison of the punch force–displacement responses implies that $\mu = 0.25$ for the Coulomb friction law is the appropriate value, and confirms that the simulated structural response is not sensitive to the choice of either solid or shell element.

While this value of friction coefficient is quite high, it is not unrealistic. In forming processes, the local friction coefficient depends on a variety of factors such as the local contact pressure [30], surface topology [31], real area of contact, surface straining and deformation-induced roughening, and lubrication condition [32]. For example, [32] implemented a boundary friction model for the simulation of a deep-drawing process and found that the predicted local friction coefficients varied among different areas of the tool from 0.1 to 0.45. The identified friction coefficient of 0.25 can be considered as an equivalent value, averaged from local ones, for the entire tool-blank interface. The possible effect of this uniform distribution assumption on the numerical predictions, such as the thickness distribution and wrinkling behavior, is still not clear, and remains to be investigated in the future.

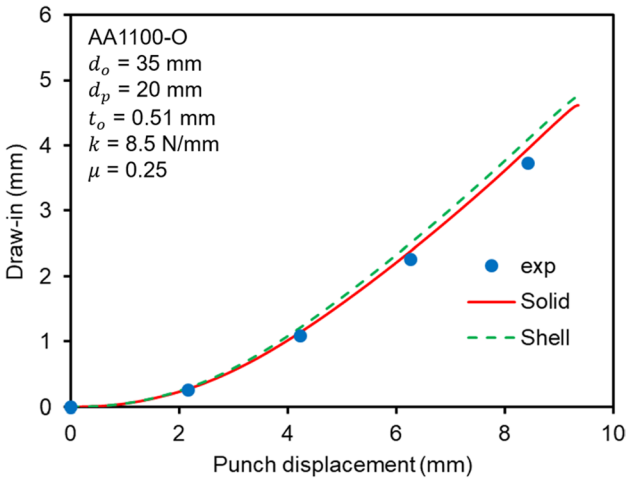

Fig. 12 Draw-in of the flange vs. punch displacement from the measurements, and predictions from solid and shell models with a friction coefficient of 0.25

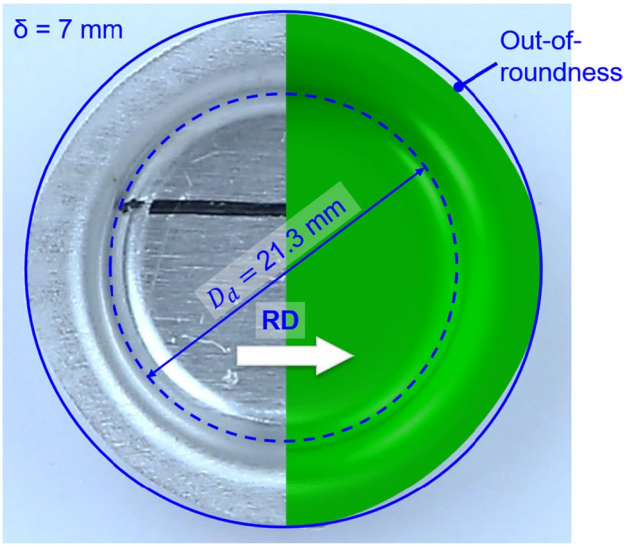

Fig. 13 Top-down view of a partially-drawn cup (left) at the punch displacement of 6 mm and the prediction (right) from shell model with a friction coefficient of 0.25

Validation of modeling framework

Comparison of flange draw-in

As a first validation of the use of $\mu = 0.25$ in the present deep-drawing simulations, the draw-in of the flange of the blank is examined. Figure 12 shows the measured draw-in in the RD, at punch displacements of 2.16, 4.23, 6.25 and 8.42 mm (blue dots). Included are the continuous evolution of the draw-in along the RD with the draw depth from the solid (solid red line) and shell models (dashed green line), where $\mu = 0.25$ is used in both models. The solid model is in good agreement with the experiments (slightly higher for the draw depth of 8.42 mm), indicating that the use of $\mu = 0.25$ in the simulations is appropriate. By contrast, the draw-in predicted by the shell model slightly overestimates the experiments beyond the draw depth of 4.23 mm, with the overestimation becoming more and more significant as the draw depth increases.

For completeness, Fig. 13 compares the partially-drawn cups from the experiment and simulation (solid elements) at a draw depth of 7 mm. The draw-in of the flange varies slightly along the circumferential direction due to the material anisotropy. The simulated shape of the flange is in good agreement with the experimental one, indicating that the FE model is capturing the material anisotropy well.

Comparison of thickness variation

In addition to the flange draw-in, the thickness variation at different draw depths is investigated to further enhance the confidence in the friction coefficient of $\mu = 0.25$ used in the simulations. Figure 14 shows the measured thickness distribution (blue lines) along the RD from the center of the blank outwards, for the draw depths of 2, 4, 6 and 8 mm. (Details of the thickness measurements can be found in Sect. 2.5.2. Note that these are different experiments than those shown in Fig. 12, i.e., the displacements are not identical.) The coordinate of the middle surface refers to the arc length along the meridian. Included are the predicted thickness variations from solid (solid red lines) and shell models (dashed green lines).

For the draw depth of 2 mm, the draw-in is very limited and the blank is essentially under bending-dominated loading, which is manifested by the two reduced thickness regions near the punch and die radii. For this case, the predictions of the solid and shell models are almost identical to each other, both capturing the nearly uniform thickness at the bottom of the cup but over-predicting the thickness towards the blank rim. This over-prediction may also be attributed to measurement errors when the deformation is relatively small.

For the draw depth of 4 mm, the draw-in becomes more pronounced, which is manifested by the thickness increase in the flange (beyond radial coordinate of 12 mm). The localized thinning becomes more significant near the punch corner radius, due to combined bending and stretching. This feature is captured successfully by the solid model. On the contrary, the shell model is not as good in the prediction of the localized thinning and its gradient near the punch corner radius.

Similar comments can be made for the draw depths of 6 and 8 mm, where the localized thinning becomes more and more significant near the punch corner radius and the flange gets thicker as more material is drawn inwards. The solid model predicts the thickness variation reasonably well, but the shell model severely underestimates the thinning near the punch corner radius and somewhat overestimates the thickening in the flange. The larger error of using a shell model to predict the draw-in can be related to the inaccurate prediction of the thickness distribution at larger draw depths. It is also noted that the experimental results shown in Fig. 14 show a trend different from the numerical ones, at the top of the vertical wall. The simulated thickness increases with the coordinate while the experimental results show an almost constant value. This can be related with the pinching of the ears in the experiments, as shown in Figs. 3c and 15a, as the downward movement of the BH is not limited by using a stopper.

It should be noted that tearing of the cup will occur around the punch corner radius if blanks with larger diameters are attempted. In that sense, the shell element model is expected to be deficient in predicting the failure in the drawing simulation.

The comparison of the thickness variation serves as another verification of using $\mu = 0.25$ in our deep-drawing simulations. The predictions of the solid model with $\mu = 0.25$ matches the experimental punch force–displacement response, draw-in and thickness variations well; the shell model with $\mu = 0.25$ performs well in matching the force–displacement response but less so for the latter two aspects. Given that the shell model is computationally less

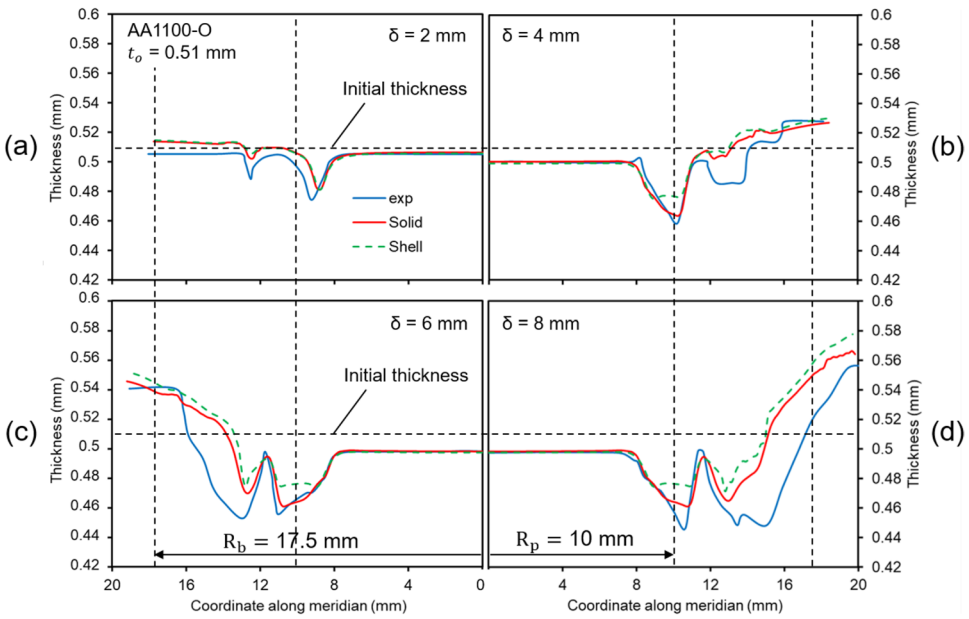

Fig. 14 Thickness distributions of the blank along the meridian of the rolling direction (using symmetry) at four different draw depths from the measurements, and predictions using solid and shell models with friction coefficient of 0.25

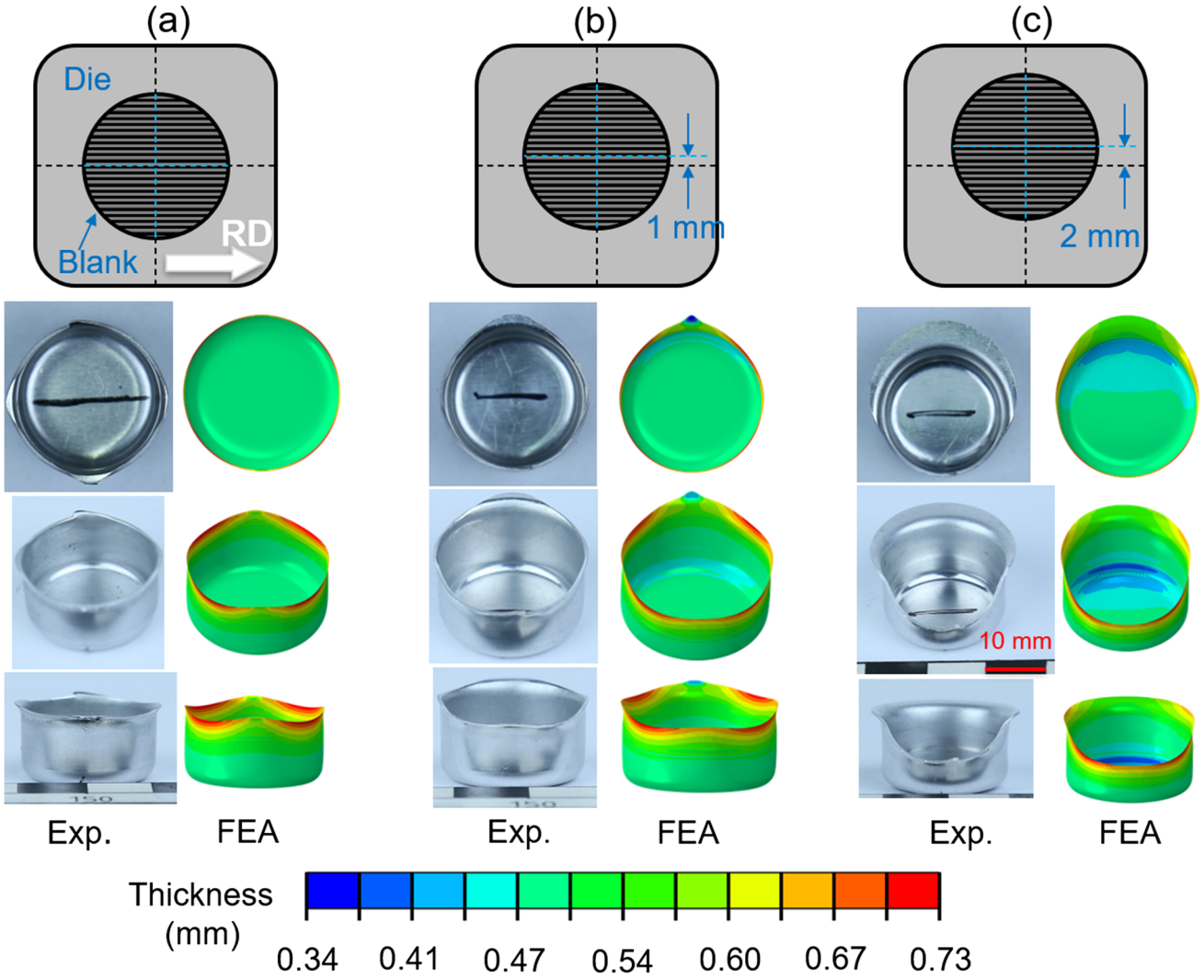

Fig. 15 Schematics of the initial position of the blanks (top row) and snapshots of the drawn cups from different perspectives from experiments and simulations for three different offset values: (a) zero offset; (b) 1 mm; (c) 2 mm

expensive than the solid model, it is favorable to use the former in the prediction of the force–displacement response and only invoke the latter when tearing predictions are of interest.

Robustness of FE model

The validation process in Sect. 4 indicates that the solid model with $\mu = 0.25$ performs the best in the deep-drawing simulations with a blank of diameter of 35 mm. In a real deep-drawing process, all inputs to the process will have both random and systematic variations. For example, blanks with somewhat different sizes, and different deviations from circularity, will be used in the drawing process, while at same time the tooling will wear out, the temperature will rise, the lubrication condition will vary, etc. Whether a FE model calibrated by using one set of process parameters still applies to the other sets remains a question, and indeed the main focus of this paper. This section investigates the robustness of the FE models to process parameter variations that may be encountered in drawing and stamping. The procedure is to evaluate the model under different off-design conditions (e.g., non-circular blanks) while keeping all the model parameters (e.g., friction, material model) the same, and establish if and when its predictions deteriorate.

Initial offset of blank center

In an actual deep-drawing process, while the blank dimensions can be systematically uniform, the blank may initially be offset from the tooling, which may not be easily controlled, particularly after the preloading of the BH. For circular blanks that are commonly encountered in

deep-drawing, the initial offset of the blank center may result in asymmetric loading and thus product geometry. Here we investigate two cases with initial offset for a blank with a diameter of 35 mm. A schematic of the initially offset blanks is shown in Fig. 15 (top row). The initial offset is assigned transversely to the RD of the blanks. Figures 15a, b and c show the snapshots of cups drawn from 0, 1 and 2 mm initially offset blanks (or 0, 2.9%, and 5.8%, respectively, of the blank diameter) from experiments and simulations, where the superimposed contours on FEA snapshots denote the thickness distribution. The height of the cups on the opposite side of the offset direction decreases as expected as the initial offset increases. Overall, the simulations reproduce the experimental results well, except for some local regions on the flange where the pinching is significant. Figure 16 shows the measured punch force–displacement responses for the two offset cases (solid lines) up to the draw depth of 10 mm. It should be noted that since the two curves are relatively close, and considering experimental error, in actual deep-drawing it would be very difficult to detect the presence of an offset merely by recording these curves.

Included in Fig. 16 are the corresponding responses from the shell model with $\mu = 0.25$. As we have demonstrated in Sect. 4.1, the shell model performs equally well as the solid model in predicting the punch force–displacement response. Therefore, the shell model is chosen here, considering its low computational cost. The predicted responses show slightly lower stiffness in the ascending part but overall they agree well with the experiments, including the successful capture of the maximum forces. In short, it is concluded that the model, as constructed and calibrated, can perform well when subjected to variations in the blank position.

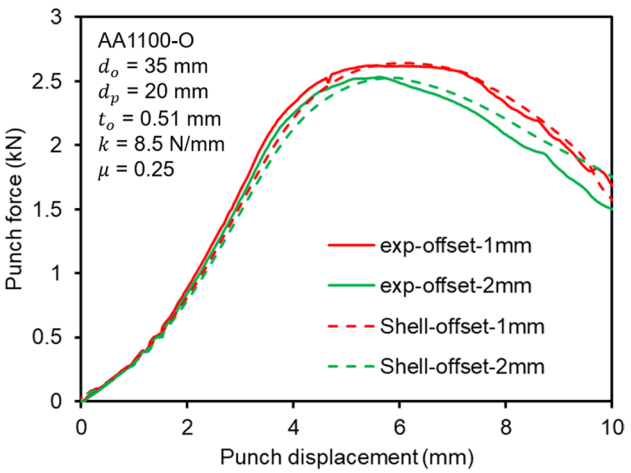

Fig. 16 Punch force–displacement responses from the measurements, and predictions using shell model for the 1 mm and 2 mm offset cases

Elliptical blank

The elliptical blank case is used as a second verification example of the robustness of the constructed FE model. The blank has a minor diameter of 35 mm in the RD and a major diameter of 41 mm in the transverse direction, see Fig. 17a. The cup drawn from this blank is shown in Fig. 17b. For comparison, the corresponding snapshots of the cups from FEA are shown in Fig. 17c, where the superimposed contours denote the thickness distribution. Overall,

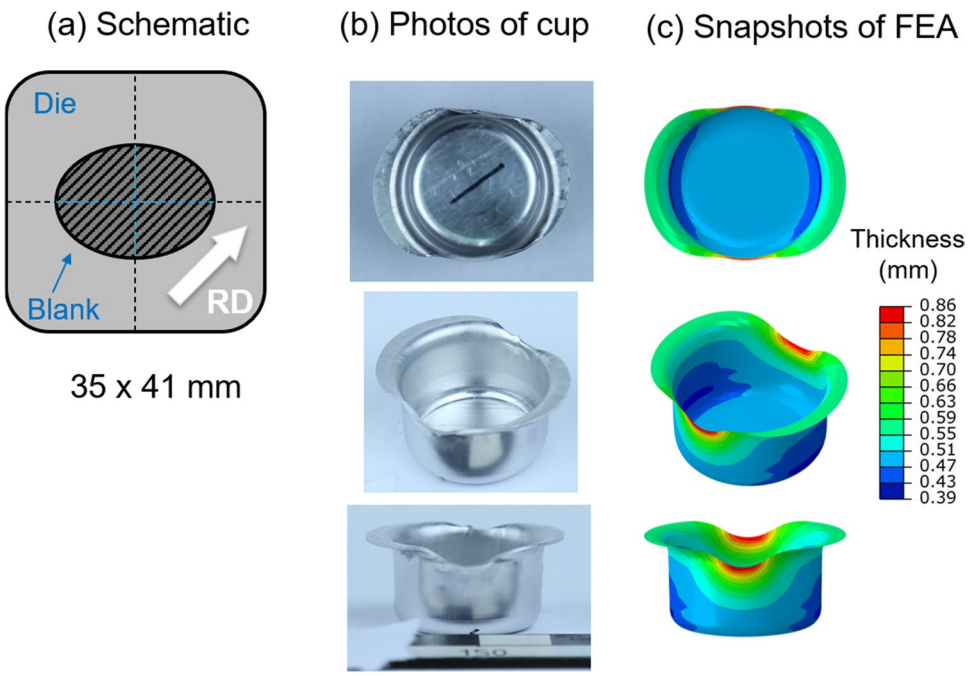

Fig. 17 (a) Schematic of the elliptical blank and material orientation; (b) photos of the drawn cups from different perspectives; (c) snapshots of the simulated cups from different perspectives

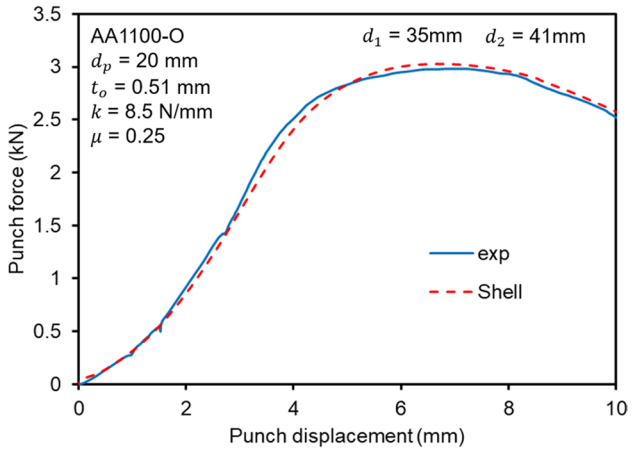

Fig. 18 Punch force–displacement responses from the measurements, and prediction using shell model for elliptical blank

the comparison of the experimental and simulated results is favorable. Figure 18 shows the measured punch force–displacement response (solid line) up to a maximum draw depth of 10 mm. Included for comparison is the response from the shell model with $\mu = 0.25$. The prediction agrees quite well with the experiment including the ascending part, the maximum force and the descending part of the response.

Different blank holder forces

Sections 5.1 and 5.2 investigated the sensitivity of the model to variations in the geometry of the blanks while the tooling, and thus the BHF, remained unchanged. This type of geometric variation results in a change of the flange area. With the current blank holder force that linearly increases with the draw depth, all the blanks with variations could be successfully drawn without failure. At the same time, the shell FE model performs reasonably well in predicting the punch force–displacement responses.

However, for process variations that involve the tooling, and may lead to a significant change of the BHF, the blanks may not be fully drawn into cups without failure, such as tearing or wrinkling. For such cases, the deformation pattern of the blank is different from that of the regularly drawn cup as it involves new physical mechanisms, such as instabilities. The FE models described thus far cannot capture these mechanisms as constructed.

This section investigates the process simulation robustness with regard to the BHF, using circular blanks with a diameter of 35 mm. Two cases with constant BHF are considered: the zero (i.e., no BH) and the 55 N BHF (i.e., the self-weight of the BH) cases. To accomplish the latter, the BH springs (see Fig. 2a) are removed, so the BH rests on the blank throughout the process and is free to move vertically.

Due to the insufficient BHF, the flange wrinkles in both cases. These wrinkled cups are shown in Fig. 19a and b, for the zero and 55 N BHF cases, respectively. As is well-established in the forming literature, the zero BHF case leads to the formation of few (in this case, four) wrinkles [33–35]. On the other hand, the 55 N BHF case leads to a significant increase in the wavenumber (in this case, from four to twelve). The previously mentioned solid and shell models fail to predict the responses and the flange wrinkling. In the zero BHF case, a shell element model may or may not show wrinkling, depending on the mesh density and element type. Furthermore, the occurrence of wrinkling can also be related to the numerical errors introduced by the FE software, e.g., when handling and storing real numbers; no matter how small these truncation errors may be, they artificially perturb the geometry of the system and may eventually trigger wrinkling. In the 55 N BHF case, no wrinkling is observed for either shell or solid elements.

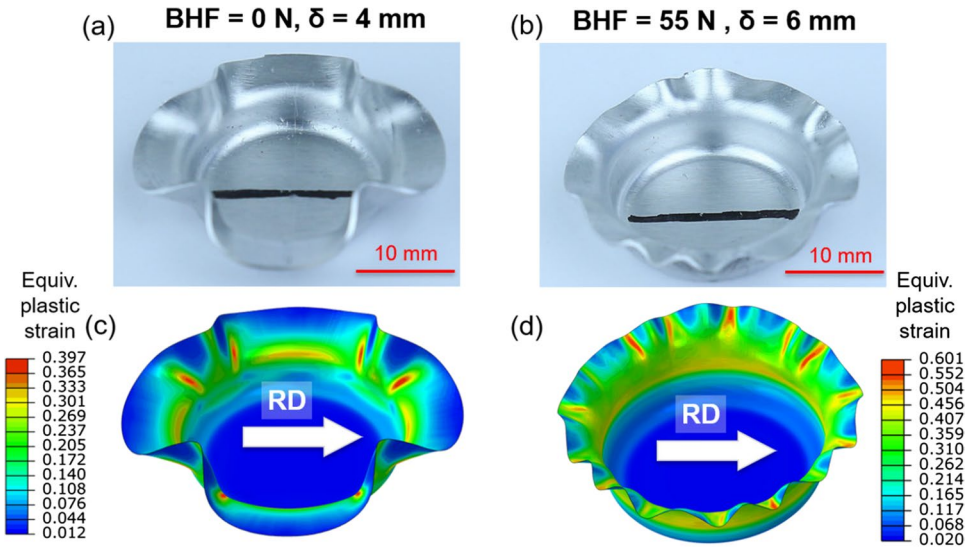

Fig. 19 Photos of the wrinkled cups under (a) zero BHF and (b) 55 N BHF, (c) and (d) snapshots of the predictions using shell model for the same cases, respectively. The superimposed contour represents the equivalent plastic strain of the top surface. The contour scale is different for the two cases

In an attempt to capture the wrinkling phenomenon in a computationally-efficient way, the shell model is chosen to be updated. This is done by expanding the quarter blank to a full size and introducing an initial geometric imperfection [36–38]. The full blank is simulated because the wrinkling may not occur periodically and thus the wrinkled cup may not continue to retain twofold symmetry. To trigger the expected flange wrinkling as shown in Fig. 19a and b, we introduce an out-of-plane offset to the nodes in the undeformed flange region. The offset value is assumed to increase linearly, from zero at the die opening radius to a maximum at the edge of the blank along each radial column of nodes. Without knowing the wrinkling wave number a priori, the out-of-plane offset amplitude at the edge of the blank is randomly assigned a value within $\pm$ 2% of the initial thickness of the blank. This leads to the random distribution shown in Fig. 20a. The entire blank with the introduction of the imperfection is also shown in Fig. 20b, where the out-of-plane amplitude is amplified 30 times, for a better visualization of the imperfection.

The updated shell model with the previously identified Coulomb friction coefficient of 0.25 is used to simulate the two constant BHF cases. Figure 21 compares the

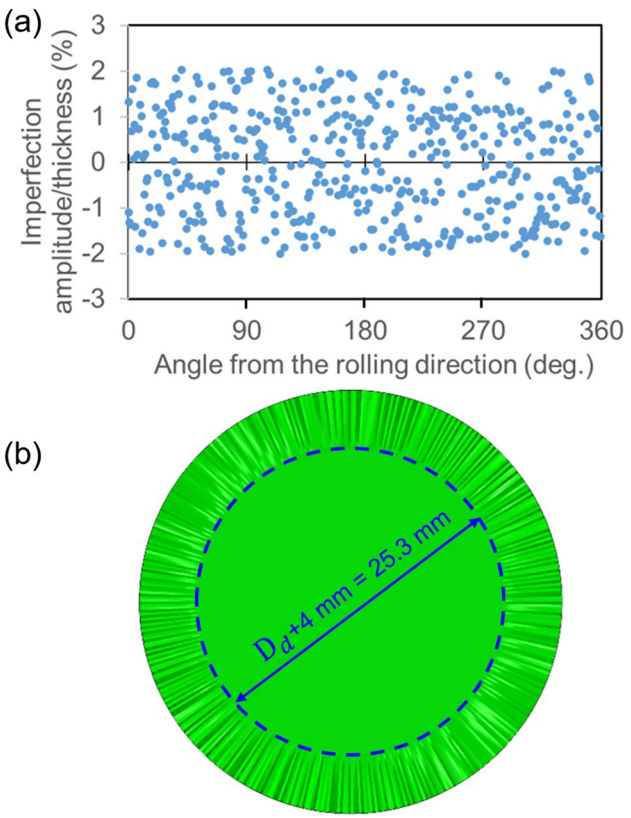

Fig. 20 (a) Random distribution of the imperfection amplitudes (normalized by the blank thickness) along the circumferential direction, at the outer periphery of the blank. (b) Top-down view of the blank with initial imperfection, the amplitudes of which are amplified 30 times for better visualization

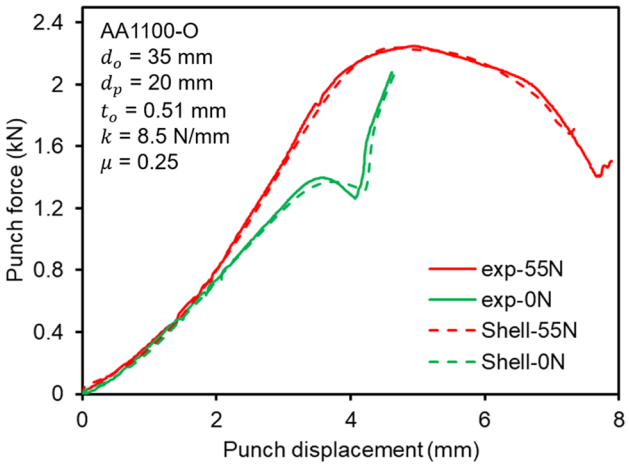

Fig. 21 Punch force–displacement responses from the measurements, and predictions using shell model (with the introduction of imperfections) for zero BHF and 55 N BHF cases

punch force–displacement responses from the simulations (dashed lines) and the experiments (solid lines) for both cases. The predicted responses from the simulations are in good agreement with the experimental ones in all aspects. The responses for zero and 55 N BHF cases are almost identical before the punch displacement reaches 2 mm. This is because in this regime the draw-in of the blank is relatively small and the blank is essentially under bending-dominated loading. Beyond a punch displacement of 2 mm, the response of the zero N case deviates from the 55 N case and traces a lower punch force level, which is attributed to the onset of flange wrinkling. As the wrinkling evolves, a locally maximum force of 1400 N develops at the punch displacement of 3.5 mm for the zero N BHF case. After a slight decrease from the maximum force, the punch force rises drastically due to the ironing of the wrinkles by the die [5, 29]. The onset of flange wrinkling for the 55 N BHF case occurs at the punch displacement of about 3.4 mm. As the wrinkle evolves, the punch force develops a maximum force of 2250 N at the displacement of 4.8 mm, and then decreases until the wrinkles block further drawing.

Four wrinkling waves are observed for the zero N case, as shown in Fig. 19a, where the marked blank line indicates the RD of the sheet. This is reproduced by the FE model, as shown in Fig. 19c, where the superimposed contour indicates the equivalent plastic strain at the draw depth of 4 mm. For the 55 N case, 12 waves are observed at the draw depth of 6 mm due to the higher BHF (see Fig. 19b), while the simulation produces 15 waves (see Fig. 19d). The disagreement here requires future study on the wrinkling mechanism of the flange under the restraint of a constant non-zero BHF [39–41]. It should be emphasized that the same geometry with random imperfection is used for the FE predictions in both cases. A different set of random imperfection is also

used in the simulations and the generated wrinkling wave numbers remain the same for both BHF cases.

In summary, this section established the fact that the FE models described in Sects. 3 and 4 are sufficiently robust against perturbations of the process parameters, provided that these do not excite new physics during the process, i.e., a behavior that is not considered when the FE models are constructed. For example, when the position or shape of the blank is altered, the FE models are robust enough to provide accurate predictions without any need for modifications. On the other hand, when the possibility of a new physical mechanism of deformation (i.e., wrinkling) is introduced, the models fail to perform as desired, until properly updated. This observation can guide the selection of appropriate process models, to enable effective process control.

Conclusions and outlook

This work reveals the need and an approach for an extended validation procedure for deep-drawing FE models used for process robustness and control investigations. Models for these investigations do not only need to predict the process result correctly when nominal values of the process parameters exist, but also when perturbations in the process conditions occur. The proposed evaluation procedure makes use of easy to perform physical tests, which do not require costly tool modifications. For demonstration purposes, the numerical modeling of the deep-drawing process of AA1100-O blanks using a 3D Servo Press is studied. Of particular interest is the robustness of the FE model to process parameter variations, such as the geometry of the blank and the BHF. The plastic anisotropy of the material is modeled using Yld2000-2d and Yld2004-18p yield functions with a combination of isotropic strain-hardening by Voce law. These material models are incorporated in shell and solid FE models, respectively. The Coulomb friction coefficient of 0.25 is inversely identified by comparing the experiment and simulation results with respect to punch force–displacement response, the draw-in and the thickness variation of the cup. The robustness of the calibrated model is tested using a series of process parameter variations, e.g., an initial offset of the blank center, elliptical blanks and different BHFs. For the zero N and 55 N BHF cases, the FE model has to be updated by introducing initial geometric imperfections to capture the wrinkling of the flange. Below are conclusions drawn from this study:

- Successful numerical modeling of deep-drawing process requires the material properties to be well characterized, including the material hardening at large strains and the plastic anisotropy.
- The friction coefficient between the blank and the tooling plays a crucial role in the simulations of deep-drawing process and must be carefully identified. The friction coefficient in this study is inversely identified by comparing the predicted and measured punch force–displacement response, draw-in and thickness variation.
- The predicted punch force–displacement response does not strongly depend on the choice of either solid or shell elements, but the draw-in and thickness variation are more sensitive. The solid model performs slightly better than the shell element in the prediction of draw-in, and significantly better for the localized wall thinning.
- A well-calibrated FE model can successfully predict the experiments with process variations in the geometry of the blank, e.g., the initial offset of the blanks and elliptical blanks.
- For process variations that lead to significant changes of the physical mechanisms, e.g., if the deformation pattern of the blank changes significantly due to new mechanisms such as wrinkling due to insufficient BHF, the FE model must be updated accordingly to capture the new deformation modes (e.g., introducing imperfections to trigger wrinkling). Once incorporated, the base model is able to predict the wrinkling behavior accurately.

Once accurate and robust numerical simulations are developed, these can be incorporated into model-based, closed-loop control of deep-drawing processes [43], e.g., using the 3D Servo Press from this research. The robust and validated numerical simulations can be used to determine appropriate actuator adjustments to assure the final part quality and characteristics are achieved even when the process is subjected to unavoidable uncertainties. Note that while key potential variations in process parameters are studied in this work, other uncertainties exist, e.g., material properties and lubrication conditions, just to list two. Thus, further research in this regard is desirable.

Supplementary Information The online version contains supplementary material available at https://doi.org/10.1007/s12289-022-01695-3.

Acknowledgements This research was supported by NSF award CMMI-1727490 and DFG award 386415239. This support is acknowledged with thanks.

Declarations

Conflict of interest The authors declare that they have no conflict of interest.

References

1. Volk W, Groche P, Brosius A, Ghiotti A, Kinsey BL, Liewald M, Madej L, Min J, Yanagimoto J (2019) Models and modelling for process limits in metal forming. CIRP Ann 68:775–798

2. Strano M, Burdi A (2007) Classification of problems under uncertainty, in fem-based analysis and design of sheet metal forming operations. In: Key Engineering Materials. Trans Tech Publ, pp 817–824
3. Alavala CR (2016) Effect of Temperature, Strain Rate and Coefficient of Friction on Deep Drawing Process of 6061 Aluminum Alloy. Int J Mech Eng 5:11–24
4. Kim H, Altan T, Yan Q (2009) Evaluation of stamping lubricants in forming advanced high strength steels (AHSS) using deep drawing and ironing tests. J Mater Process Technol 209:4122–4133
5. Tian H, Brownell B, Baral M, Korkolis YP (2017) Earing in cup-drawing of anisotropic Al-6022-T4 sheets. Int J Mater Form 10:329–343. https://doi.org/10.1007/s12289-016-1282-y
6. Coer J, Laurent H, Oliveira MC, Manach P-Y, Menezes LF (2018) Detailed experimental and numerical analysis of a cylindrical cup deep drawing: pros and cons of using solid-shell elements. Int J Mater Form 11:357–373
7. Yalçın S (2010) Analysis and modeling of plastic wrinkling in deep drawing
8. Vrh M, Halilovič M, Starman B, Štok B, Comsa D-S, Banabic D (2014) Capability of the BBC2008 yield criterion in predicting the earing profile in cup deep drawing simulations. Eur J Mech - A/Solids 45:59–74. https://doi.org/10.1016/j.euromechsol.2013.11.013
9. Yoon J-W, Barlat F, Dick RE, Chung K, Kang TJ (2004) Plane stress yield function for aluminum alloy sheets—part II: FE formulation and its implementation. Int J Plast 20:495–522. https://doi.org/10.1016/S0749-6419(03)00099-8
10. Moreira LP, Ferron G, Ferran G (2000) Experimental and numerical analysis of the cup drawing test for orthotropic metal sheets. J Mater Process Technol 108:78–86. https://doi.org/10.1016/S0924-0136(00)00660-9
11. Barrett TJ, Knezevic M (2019) Deep drawing simulations using the finite element method embedding a multi-level crystal plasticity constitutive law: experimental verification and sensitivity analysis. Comput Methods Appl Mech Eng 354:245–270
12. Neto DM, Oliveira MC, Dick RE, Barros PD, Alves JL, Menezes LF (2017) Numerical and experimental analysis of wrinkling during the cup drawing of an AA5042 aluminium alloy. Int J Mater Form 10:125–138
13. Zhuang S (2008) Enhancing Implicit Finite Element Sheet Forming Simulation. Doctoral Dissertation, The Ohio State University
14. Pelz PF, Groche P, Pfetsch M, Schäffner M (2021) Mastering Uncertainty in Mechanical Engineering
15. Padmanabhan R, Oliveira MC, Alves JL, Menezes LF (2007) Influence of process parameters on the deep drawing of stainless steel. Finite Elem Anal Des 43:1062–1067
16. Thuillier S, Manach PY, Menezes LF, Oliveira MC (2002) Experimental and numerical study of reverse re-drawing of anisotropic sheet metals. J Mater Process Technol 125:764–771
17. Yoon JW, Barlat F, Dick RE, Karabin ME (2006) Prediction of six or eight ears in a drawn cup based on a new anisotropic yield function. Int J Plast 22:174–193. https://doi.org/10.1016/j.ijplas.2005.03.013
18. Fukumasu H, Kuwabara T, Takizawa H, Yamanaka A (2018) Influence of hardening functions on earing prediction in cup drawing of AA3104 aluminum alloy sheet. In: Journal of Physics: Conference Series. IOP Publishing, p 12114
19. Comsa DS, Banabic D (2007) Numerical simulation of sheet metal forming processes using a new yield criterion. In: Key Engineering Materials. Trans Tech Publ, pp 833–840
20. Groche P, Scheitza M, Kraft M, Schmitt S (2010) Increased total flexibility by 3D Servo Presses. CIRP Ann 59:267–270
21. Hesse D, Hoppe F, Groche P (2017) Controlling Product Stiffness by an Incremental Sheet Metal Forming Process. Procedia Manuf 10:276–285. https://doi.org/10.1016/j.promfg.2017.07.058
22. Hoppe F, Pihan C, Groche P (2019) Closed-loop control of eccentric presses based on inverse kinematic models. Procedia Manuf 29:240–247. https://doi.org/10.1016/j.promfg.2019.02.132
23. Ha J, Breunig A, Fones J, Hoppe F, Korkolis YP, Groche P, Kinsey BL (2019) AA1100-O cylindrical cup-drawing using 3D servo-press. In: IOP Conference Series: Materials Science and Engineering
24. Johnson W, Mellor PB (1978) Engineering Plasticity. Van Nostrand Reinhold Company
25. Ha J, Fones J, Kinsey BL, Korkolis YP (2020) Plasticity and formability of annealed, commercially-pure aluminum: Experiments and modeling. Materials (Basel) 13. https://doi.org/10.3390/ma13194285
26. Anon (2004) ASTM E8 Standard Test Methods for Tension Testing of Metallic Materials. ASTM International, , Philadelphia
27. Barlat F, Brem JC, Yoon JW, Chung K, Dick RE, Lege DJ, Pourboghrat F, Choi S-H, Chu E (2003) Plane stress yield function for aluminum alloy sheets—part 1: theory. Int J Plast 19:1297–1319. https://doi.org/10.1016/S0749-6419(02)00019-0
28. Barlat F, Aretz H, Yoon JW, Karabin ME, Brem JC, Dick RE (2005) Linear transfomation-based anisotropic yield functions. Int J Plast 21:1009–1039. https://doi.org/10.1016/j.ijplas.2004.06.004
29. Lange K (1985) Handbook of metal forming. McGraw-Hill
30. Gil I, Mendiguren J, Galdos L, Mugarra E, de Argandoña ES (2016) Influence of the pressure dependent coefficient of friction on deep drawing springback predictions. Tribol Int 103:266–273
31. Zabala A, Galdos L, Childs C, Llavori I, Aginagalde A, Mendiguren J, Saenz de Argandoña E (2021) The Interaction between the Sheet/Tool Surface Texture and the Friction/Galling Behaviour on Aluminium Deep Drawing Operations. Metals (Basel) 11:979
32. Shisode M, Hazrati J, Mishra T, de Rooij M, ten Horn C, van Beeck J, van den Boogaard T (2021) Modeling boundary friction of coated sheets in sheet metal forming. Tribol Int 153:106554
33. Senior BW (1956) Flange wrinkling in deep-drawing operations. J Mech Phys Solids 4:235–246
34. Yu TX, Johnson W (1982) The buckling of annular plates in relation to the deep-drawing process. Int J Mech Sci 24:175–188
35. Chu E, Xu Y (2001) An elastoplastic analysis of flange wrinkling in deep drawing process. Int J Mech Sci 43:1421–1440
36. Timoshenko SP, Gere JM (1961) Theory of elastic stability. McGraw-Hill
37. Brush DO, Almroth BO (1975) Buckling of bars, plates, and shells. McGraw-Hill
38. Cao J, Boyce MC (1997) Wrinkling behavior of rectangular plates under lateral constraint. Int J Solids Struct 34:153–176
39. Chen K, Korkolis YP (2020) Industry 4.0 in stamping: A wrinkling indicator for reduced-order modeling of deep-drawing processes. Procedia Manuf 51:864–869
40. Chen K, Korkolis YP (2021) A simplified model of elastic column buckling under constant lateral force restraint. Arch Appl Mech 91:2817–2832
41. Chen K, Korkolis YP (2021) Buckling and Post-Buckling of an Elastica Under a Lateral Restraining Force. Int J Solids Struct 111178
42. Groche P, Hoppe F, Sinz J (2017) Stiffness of multipoint servo presses: Mechanics vs. control. CIRP Ann 66:373–376. https://doi.org/10.1016/j.cirp.2017.04.053
43. Allwood JM, Duncan SR, Cao J et al (2016) Closed-loop control of product properties in metal forming. CIRP Ann 65:573–596